An Atmospheric Signal Lowering the Spring Predictability Barrier in Statistical ENSO Forecasts

Dmitry Mukhin[1,1], Andrey Gavrilov[1,1], Aleksei Seleznev[1,1], and Maria Buyanova[1,2]

[1]Institute of Applied Physics of the Russian Academy of Sciences
[2]Institute of Applied Physics

November 30, 2022

Abstract

The loss of autocorrelations of tropical sea surface temperatures (SST) during late spring, also called the spring predictability barrier (SPB), is a factor that strongly limits the predictability of El Nino Southern Oscillation (ENSO), and especially the statistical SST-based ENSO forecasts starting from the winter-spring season. Recent studies show that Pacific atmospheric circulation anomalies in winter-spring may have a long-term impact on the summer tropical climate via the SST footprint. Here, we infer an index based on sea level pressure (SLP) data from February-March in a single area surrounding Hawaii, and show that this area is the most informative part of the large SLP pattern initiating the SST footprinting mechanism. We then construct a statistically optimal linear model of the Nino 3.4 index taking this atmospheric index as a forcing. We find that this forcing efficiently lowers the SPB and provides significant improvements of interseasonal Nino 3.4 forecasts.

An Atmospheric Signal Lowering the Spring Predictability Barrier in Statistical ENSO Forecasts

Dmitry Mukhin[1,2], Andrey Gavrilov[1,2], Aleksei Seleznev[1,2], and Maria Buyanova[1]

[1]Institute of Applied Physics of the RAS, Nizhny Novgorod

[2]Research and Education Mathematical Center "Mathematics for Future Technologies", Nizhny Novgorod State University

Key Points:

- A novel early ENSO predictor based on the February-March SLP is introduced
- Significant correlations of the predictor with the upcoming summer - next spring ENSO conditions are shown
- The predictor significantly improves the interseasonal forecast skills of the statistical Niño 3.4 index model

Corresponding author: Dmitry Mukhin, mukhin@ipfran.ru

Abstract

The loss of autocorrelations of tropical sea surface temperatures (SST) during late spring, also called the spring predictability barrier (SPB), is a factor that strongly limits the predictability of El Nino Southern Oscillation (ENSO), and especially the statistical SST-based ENSO forecasts starting from the winter-spring season. Recent studies show that Pacific atmospheric circulation anomalies in winter-spring may have a long-term impact on the summer tropical climate via the SST footprint. Here, we infer an index based on sea level pressure (SLP) data from February-March in a single area surrounding Hawaii, and show that this area is the most informative part of the large SLP pattern initiating the SST footprinting mechanism. We then construct a statistically optimal linear model of the Nino 3.4 index taking this atmospheric index as a forcing. We find that this forcing efficiently lowers the SPB and provides significant improvements of interseasonal Niño 3.4 forecasts.

Plain Language Summary

Interseasonal forecasting of El Niño Southern Oscillation (ENSO) is in high demand due to the impacts of ENSO on regional climatic conditions around the world as well as the global climate. Improvements in the quality of climate data in recent decades have led to the active use of statistical ENSO models, which compete with physical models in predictive power. The main disadvantage of statistical forecasts is the pronounced seasonal growth of uncertainty when predicting the upcoming summer-fall ENSO conditions from winter-spring months; this phenomenon is called the spring predictability barrier (SPB). A number of recent works revealed that winter-spring atmospheric anomalies can substantially impact the ENSO system through the SPB via a complex atmosphere-ocean interaction mechanism. Here, we introduce a reliable ENSO predictor constructed from sea level pressure data relating to this mechanism and show that the predictor significantly improves the multimonth (up to one year) ENSO forecast by lowering the SPB in a statistical model of the key ENSO index.

1 Introduction

Statistical models are known to be simple and effective tools for interseasonal predictions of ENSO dynamics (Barnston et al., 2012; Jan van Oldenborgh et al., 2005). The IRI/CPC ENSO Predictions Plume (Barnston et al., 2012) — an ensemble forecast of the Niño 3.4 index defined as the average SST in the region (5°N-5°S, 170°W-120°W) — demonstrates that both statistical and dynamical models yield close prediction skills at lead times up to 12 months. This similarity likely reflects the near-linearity of the seasonal tropical Indo-Pacific SST predictability studied by Newman and Sardeshmukh (2017). The main factor limiting statistical forecasts is the spring predictability barrier (SPB), also called the spring persistence barrier, i.e., the empirically observed loss of autocorrelations in the tropical Pacific climate dynamics in May-June (Torrence & Webster, 1998; Barnston et al., 2012). Since many statistical models rely on SST anomalies (SSTAs) in the tropics, the SPB impacts statistical models more than dynamical models during forecasts beginning in spring (Barnston et al., 2012). Basically, the SPB phenomenon can be explained as a manifestation of ENSO seasonality related to the phase locking of ENSO dynamics with a seasonal cycle (Liu et al., 2018). In the tropical SSTA variability, there is a distinct one-year temporal pattern (cycle) that lasts from June to May of the following year, with persistent SST anomalies developing in the middle of the cycle (autumn-winter), whereas smaller and noisier anomalies appear at the beginning and end of the cycle (summer and spring, respectively). In particular, Tippett and L'Heureux (2020) recently showed that approximately 90% of the Niño 3.4 index variability can be explained by a 1-dimensional deterministic signal defined on the June-May interval multiplied by different amplitudes in different years, with extrema in December and the lowest absolute values in May and June. As a result of this seasonality, spring SSTAs are strongly influenced by atmospheric noise and therefore yield little information for predicting SSTAs in the next cycle. Finding effective predictors that can bridge adjacent cycles and thus avoid the SPB remains a challenging task in ENSO predictive modeling.

Oceanic predictors play a central role in statistical ENSO models. An upper ocean heat content in the tropics characterized by, e.g., a warm water volume along the equator, is widely thought to be one of the earliest predictors for ENSO-related anomalies (McPhaden, 2003; Timmermann et al., 2018). This predictor exhibits no persistence barrier in boreal spring but leads the tropical SST by several months (McPhaden, 2003). The latter is consistent with the recharging oscillator (Burgers et al., 2005; Jin, 1997) and delayed oscillator (Suarez & Schopf, 1988; Galanti & Tziperman, 2000) models of ENSO, both reflecting ocean-atmosphere feedback loops, which imply lagged interconnections between the SST and thermocline. The models based on pure SST analyses (e.g., (Kondrashov et al., 2005; Gavrilov et al., 2019)) can capture the impact of this factor by increasing the depth of memory: series of lagged SSTs used to initialize such models contain information on SST tendencies that, in turn, depend on anomalies of the upper ocean heat content, as noted by Tippett and L'Heureux (2020). However, the ENSO oscillatory structure is significantly complicated by ENSO-independent atmospheric anomalies acting as a forcing, which can alter the zonal wind stress over the equatorial Pacific Ocean and trigger ENSO events (Vimont et al., 2003; Yu & Fang, 2018). Specifically, extratropical atmospheric patterns dominating in the winter season over the Pacific Ocean have a long-term impact on the whole upcoming ENSO cycle via the SST footprinting mechanism (Vimont et al., 2009, 2003). Fang and Mu (2018) argue that this mechanism needs to be considered to weaken the SPB, and both oceanic and atmospheric factors are important for long-term ENSO forecasts. Typically, the time series used for statistical ENSO model learning begin in the middle of the 20th century; i.e., the analyzed time interval covers approximately two dozen El Niño (La Niña) events. However, the significance of ENSO predictors that are somehow extracted from atmospheric data of such short duration is always questionable due to the possibility of detecting spurious correlations. Moreover, a model that takes such an extracted predictor may exhibit a good fit with the analyzed sample but be otherwise useless. Naturally, such a situation, also called overfitting, is probable when the predictor is assembled from many weakly correlated signals from different regions without relevant statistical tests. Therefore, statistical significance becomes a major issue both in deriving a useful signal from data and in studying the benefits of the model skills acquired using the predictor.

In this work, we derive an atmospheric ENSO predictor from sea level pressure (SLP) data that is useful for forecasting the Niño 3.4 index across the SBP. We introduce a February-March SLP index reflecting the footprinting mechanism that features a strong significant correlation with the Niño 3.4 index in each month during the upcoming June-May ENSO cycle. Next, we pass the index obtained as a forcing to an autoregressive (AR) model with memory and periodic coefficients that is built from the Niño 3.4 index. Bayesian hypothesis testing is employed to optimize the model, e.g., to confirm the optimality of the model with such a forcing. We show that the forcing yields a significant improvement in the model prediction skill at lead times reaching up to one year due to a substantial reduction in the SPB.

2 Atmospheric ENSO predictor

To find a pre-SPB atmospheric ENSO predictor, we use a monthly 1959–2019 SLP dataset on a 144×73 global grid taken from NCEP-NCAR Reanalysis 1 (Kalnay et al., 1996). SLP anomalies (SLPAs) are obtained from this dataset by subtracting the periodic SLP annual climatology and then applying linear detrending at each grid point. To represent ENSO dynamics, the monthly detrended 1960–2019 Niño 3.4 index is produced from the Extended Reconstructed SST (ERSST) dataset, version 5 (Huang et al., 2017a). We analyze the correlations of the SLP in the winter and spring seasons with the yearly Niño 3.4 index time series in each month of the upcoming ENSO cycle. The correlation maps for three selected ENSO months are plotted in the three upper panels of Fig. 1; a figure showing the results for all months is also provided in the Supporting Information (SI). The correlations in the central part of the Pacific Ocean are much higher for the SLP from February onward than for the SLP during December-January. Moreover, in February-March, there is a distinguishable SLP pattern surrounding Hawaii that persistently correlates with the Niño 3.4 index over the entire June-May ENSO cycle.

Fig. 1 shows only the significant correlations (based on the pairwise AR1 surrogate test) of the SLP in each grid point with the Niño 3.4 index. However, to conclude that the SLP signal at a given point actually correlates with the index, we must reject the more general null hypothesis — that an identical or higher sample correlation can appear by chance at some other point on the globe, i.e., in a random (independent of the Niño 3.4 index) sample preserving the spatiotemporal properties of the analyzed SLP sample. For this purpose, for every analyzed SLP season, we use 10000 random globally distributed yearly SLPA time series obtained by generating AR1 surrogates of the SLPA principal components (PCs) — the time series of the SLPA EOFs (see the SI). For each of the SLPA surrogates, we calculate the maximal absolute correlation with the Niño 3.4 index over all grid points. Then, the obtained ensemble of correlations is used to calculate the critical values for the correlations plotted in Fig. 1: the black contours in this figure bound the areas of significant correlations for a 0.1 significance level (the right-tailed test for absolute correlation values is applied). The results confirm the persistence of a small area near Hawaii with strong significant correlations between the February-March SLP and the upcoming Niño 3.4 index. To summarize the correlation maps for the Niño 3.4 index in different months, let us also consider the correlations of the winter-spring SLP with the upcoming ENSO cycle as a whole. According to Tippett and L'Heureux

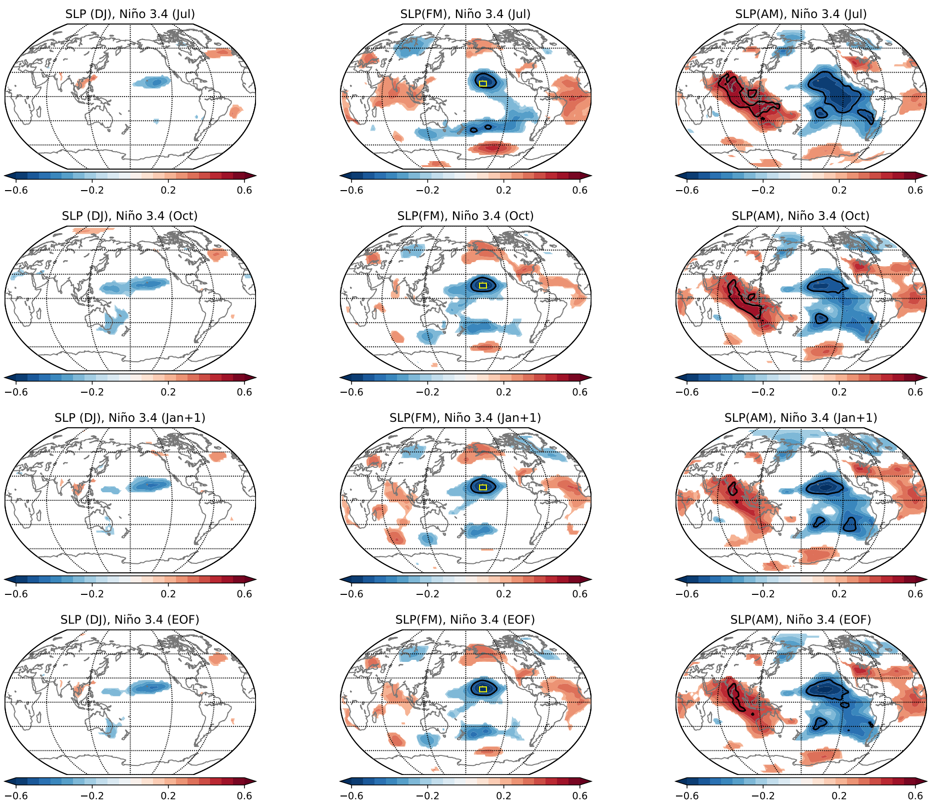

Figure 1. Correlations of the seasonal SLP means during December-January (DJ), February-March (FM) and April-May (AM) with the Niño 3.4 index in the following months. The three upper rows show the correlations with the Niño 3.4 index in July, October and January. The bottom row shows the correlations with the Niño-EOF time series characterizing the whole ENSO cycle following the considered SLP seasons. Only significant correlations (0.1 significance level) are plotted in accordance with the AR1 surrogate test applied to absolute values of the correlations in each grid point separately. The black contours correspond to the 0.1 significance level of the stronger test based on globally distributed SLPA surrogates (see the main text). The yellow rectangles mark the area used for the HI.

(2020), the ENSO cycle in the Niño 3.4 index can be represented well by the 1st leading EOF constructed from the series of 12-month nonoverlapping windows of the Niño 3.4 index time series, each starting in June. For the dataset analyzed here, this EOF (hereinafter Niño-EOF) captures approximately 88% of Niño 3.4 index variance. Hence, the projection of June-to-May intervals of the Niño 3.4 index to this EOF can be treated as a yearly time series of the ENSO cycle amplitude. The bottom row of Fig. 1 demonstrates that the area surrounding Hawaii is the only place on the globe with apparent correlations between the February-March SLP and Niño-EOF. Based on this finding, we define the Hawaiian index (HI) as the mean SLPA in the region (13°N-19°N, 150°W-160°W) averaged over February-March. The yearly time series of the HI significantly correlates with the Niño 3.4 index in all months of the ENSO cycle, as Fig. 2a demonstrates. The Niño-EOF component of the Niño 3.4 index dominates these correlations compared with other Niño 3.4 12-month EOFs (see Fig. 2a). The correlation coefficient between the HI and the upcoming ENSO cycle represented by the Niño-EOF time series is 0.66; Fig. 2b shows that moderate and strong ENSO events play the most important role in such a strong correlation.

We can determine the possible benefits of the HI in ENSO forecasting by considering the AR model constructed from the Niño 3.4 index with parameters separately estimated for each month of the year (the AR model with periodic coefficients). In Fig. 2c, we compare the mean squared errors (MSEs) of 1-month predictions given by such a model with those of the same model but complemented by the HI factor:

$$x_{ni} = a_1^i x_{ni}^{-1} + a_2^i x_{ni}^{-2} + \cdots + a_l^i x_{ni}^{-l} + b^i h_n + \xi_{ni}, \tag{1}$$

where x_{ni} is the Niño 3.4 index in the ith month of the nth ENSO cycle, x_{ni}^{-j} is the same index j months before x_{ni}, h_n is the HI value preceding the nth ENSO cycle, and l is the lag. In this notation i runs from 1 to 12, where $i = 1$ corresponds to June – the first month of the cycle. The SPB-related loss of autocorrelations clearly manifests as pronounced June peaks of the MSE $\left\langle \xi_{ni}^2 \right\rangle_n$ in the pure AR models ($b_i = 0$) with different lags (see Fig. 2c). Lags greater than 2 months hardly improve the forecast in all months of the cycle, but the addition of the HI to the lag=2 AR model leads to a substantial decrease in the June MSE peak. Thus, the SPB weakens when both the lagged SST and the HI are used together as ENSO predictors.

Now let us try to ascertain the origin of the HI factor by studying large-scale atmospheric structures over the North Pacific preceding different ENSO cycles. To this end, we construct composite patterns as the February-March SLPA averaged separately over the years of El Niño and La Niña onset. Only the years with moderate and strong ENSO events (stars in Fig. 2b) are taken to form the El Niño/La Niña-related SLPA subsamples. This criterion eliminates the uncertainties in separating out weak and neutral ENSO phases, which depends on the specific definition of the ENSO index. The resulting El

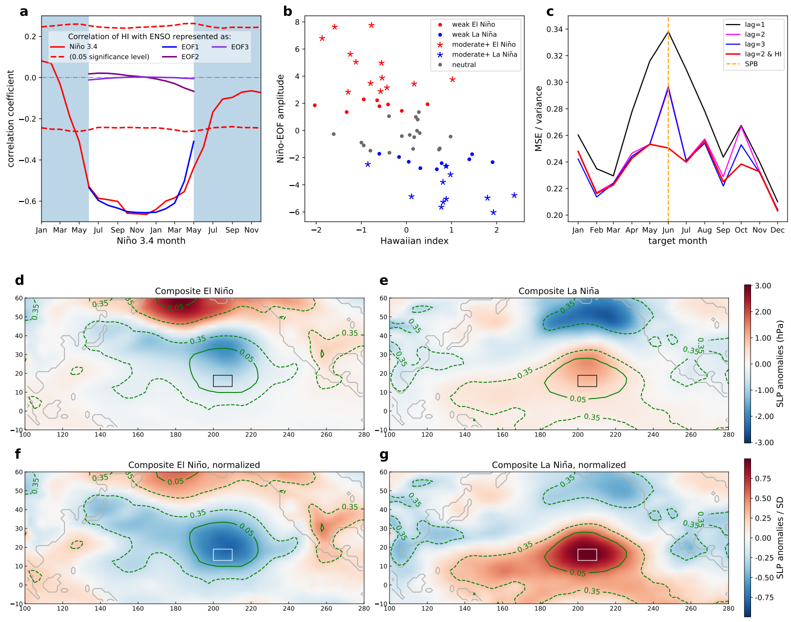

Figure 2. Relation of the February-March (FM) SLP with the Niño 3.4 index cycle. (a) Correlations of the HI with the Niño 3.4 index as a function of the Niño 3.4 month (solid red curve) and the 0.05 significance level (dashed red lines) from the AR1 two-tailed test. Niño 3.4 months run from January in the HI years to December one year ahead. Contributions of the Niño 3.4 components corresponding to three leading 12-month EOFs (see the text) are shown by blue and violet curves (see the legend). (b) ENSO cycle amplitudes vs. the HI. These amplitudes are the projections of June-May Niño 3.4 windows to the Niño-EOF. Cycles corresponding moderate and strong (moderate+), weak and neutral ENSO events (as classified by https://ggweather.com/enso/oni.htm) are plotted by stars, colored circles and black circles, respectively. Red and blue denote El Niño and La Niña phases, respectively. (c) The 1-month mean squared errors (MSEs) of the Niño 3.4 linear regressive model (1) as a function of the month. MSEs of the autoregressive ($b^i = 0$) model with $l = 1, 2, 3$ are shown by black, pink and blue, respectively. The MSE of the model depending on both the 2 previous Niño 3.4 months ($l = 2$) and the HI is shown in red. (d-g) Composite patterns of the FM SLPAs preceding El Niño events (d,f) and La Niña events (e,g). (d,e) The nonnormalized composites; (f,g) the composites normalized by the standard deviation (SD) of the FM SLPAs in each grid point. The green contours bound the significant values for significance levels of 0.05 and 0.35 (see the main text and SI). The rectangle marks the HI area.

Niño and La Niña composites are shown in Fig. 2d,e. The significance of the composites was studied by testing the null hypothesis that the multiyear means obtained could appear in random SLP dataset subsamples of the same size as the size of the investigated subsamples related to El Niño and La Niña (see the SI for details). The areas bound by the contours in Fig. 2d-g are filled with significant values at significance levels of 0.05 and 0.35 from the right-tailed test applied to the absolute values of the composites. Note that these areas do not necessarily encompass the highest absolute composite values; this is due to the nonuniform distribution of the SLP variance over the spatial grid and hence the spatially dependent distribution of the SLP means under the null hypothesis. In contrast, the contours of the significance levels coincide with the isolines of the composites normalized to the standard deviation of the February-March SLP at each grid point (see the bottom panels of Fig. 2f,g). These normalized composites outline the areas that contain the most useful information for predicting the ENSO phase in the upcoming cycle.

The El Niño and La Niña composites resemble the negative and positive patterns, respectively, of the North Pacific Oscillation (NPO). This is not surprising since the winter-spring NPO pattern initiates the subtropical SST footprint, which persists into the summer season and can impact the ENSO variability by forcing zonal wind anomalies along the equator (Vimont et al., 2003). From Fig. 2d-g, we can learn that the ENSO-related NPO-like structure is apparently asymmetric with respect to the ENSO phase: the positive pattern cannot be obtained by simply inverting the negative pattern. In particular, in the La Niña composite, the northern part of the NPO dipole is shifted eastward, while its southern part penetrates deeper into the tropics. However, the most significant region surrounds the HI area (see Fig. 2f,g), which is common for both composites. This explains the strong correlation of the HI with the ENSO cycle. Thus, we can conclude that the HI relates to the SST footprinting mechanism and actually captures the linear part of the interaction between the winter-spring NPO pattern and ENSO. Nonlinear data analysis methods, such as those of (Kramer, 1991; Mukhin et al., 2015, 2018; Gavrilov et al., 2016; Hannachi & Iqbal, 2019), could help extract a better ENSO predictor by capturing the asymmetry of the NPO pattern; nevertheless, we leave this complex task for future works and restrict our consideration to a linear analysis.

3 Niño 3.4 forecast by a forced AR model

In this section, we construct a statistically optimal model for long-term Niño 3.4 forecasting on the basis of the AR model with periodic coefficients forced by the suggested HI. The basic form of the model is given by Eq. 1: the value of the Niño 3.4 index in some month is predicted from the values in the l preceding months as well as the HI value, which is calculated once a year from the February-March SLPs and remains constant during each June-to-May interval. Thus, the HI plays the role of a piecewise uniform forcing signal that determines the "substructure" for each ENSO cycle. Physically, the HI produces seasonally dependent shifts in the predicted values during each ENSO cycle, making the model dynamics favorable for the development of El Niño or La Niña conditions. The most important point when constructing a statistical model of this kind is the optimal number of its parameters or, equivalently, the number of factors on which the model depends. Choosing the proper model structure should provide a sufficiently complex but statistically correct (i.e., not overfitted) model. In our case, the number of parameters is determined by the following structural features of the model (1). The first feature is the lag l, which limits the length of the model memory. Another feature is the periodic seasonal dependence of the factors' amplitudes a and b. In the previous section, we estimated the parameters for different months of the year independently. However, for the optimal multiseason model, smoother dependencies should be checked, including constant dependencies. Here, we use a discrete Fourier representation for the periodic series of the model coefficients $\mathbf{k}^i = \left(a_1^i, \dots a_l^i, b^i\right)$:

$$\mathbf{k}^i = \mathbf{k}_0 + \sum_{n=1}^{q} \mathbf{c}_n \cos \frac{2\pi}{12} ni + \mathbf{s}_n \sin \frac{2\pi}{12} ni, \tag{2}$$

where $i = 1, \dots, 12$, q can take values from 0 to 6 ($q = 0$ corresponds to $\mathbf{k}^i = \mathbf{k}_0$; $\mathbf{s}_6 = 0$ by definition) and $\mathbf{k}_0$, $\mathbf{c}_n$ and $\mathbf{s}_n$ are the new coefficients to be estimated. The case $q = 6$ is equivalent to 12 independently learned models corresponding to different months. Truncating the expansion (2) by the q constraint, we can adjust the smoothness of the seasonal forcing in the model parameters.

Thus, we have two structural parameters for the model, namely, l and q, the choice of which should be proven. Additionally, we have to justify that including the HI forcing h_n in the model not only fits the model to the learning sample, but improve its predictive skills. To select the optimal model, we use the Bayesian criterion of model optimality based on the method described in (Gavrilov et al., 2019, 2017). This method is also presented in the SI together with the method of Bayesian regression used for learning the model (1–2).

The model in the form of (1–2) is a stochastic evolution operator due to the random term ξ. The forecast of the index x several months ahead is produced by iterating this operator several times. As a result, the output of such a forecast is a random value with some PDF. Here, following (Gavrilov et al., 2019), we define the predicted value $\overline{x}$ as the median of this PDF, which is estimated by the Monte Carlo method with 10000 runs. Similar to Barnston et al. (2012) and Gavrilov et al. (2019), we use two metrics to represent the seasonally dependent model prediction skill based on comparing the true x_{ni} in the i-th target month of the n-th ENSO cycle with the predicted $\overline{x}_{ni}$:

$$e_i = \left[\frac{1}{N}\sum_n \left(\overline{x}_{ni} - x_{ni}\right)^2\right]^{\frac{1}{2}},$$

$$r_i = \frac{\sum_n \left(x_{ni} - \langle x_{ni}\rangle_n\right)\left(\overline{x}_{ni} - \langle \overline{x}_{ni}\rangle_n\right)}{\left[\sum_n \left(x_{ni} - \langle x_{ni}\rangle_n\right)^2 \sum_n \left(\overline{x}_{ni} - \langle \overline{x}_{ni}\rangle_n\right)^2\right]^{\frac{1}{2}}}, \tag{3}$$

where N is the total number of ENSO cycles and $\langle x_{ni}\rangle_n$ denotes the seasonal multiyear mean of the index. The first metric e_i is the root mean square (r.m.s.) forecast error in the i-th month. The second metric r_i is simply the sample correlation between the predicted and true values of the index in month i. These two metrics complement each other: while e signifies the quantitative forecast error, r reflects the qualitative features of the forecast, e.g., the tendencies of and relative changes in the predicted anomalies.

We find that the lag=2 AR model forced by both the seasonal parameter forcing and the yearly HI forcing is the best Niño 3.4 index model in accordance with the Bayesian model optimality (see the SI). The optimal truncation of the seasonal forcing (see Eq. 2) corresponds to $q = 1$; i.e., the amplitudes a and b in Eq. 1 are sinusoidal signals with a 1-year period. To study the benefits in multimonth forecasts from using both forcing signals, we compare the prediction skills of (i) the model without any forcing ($b = 0$ and $q = 0$) but with the optimal lag l, (ii) the model with the seasonal forcing only ($b = 0$) and with the optimal l and q, and (iii) the optimal model with the combined forcing. The results are summarized in Fig. 3a, where the metrics (3) of the model prediction skill are plotted for lead times of up to one year.

Note that for any target month i, the HI forcing is available only for a limited lead time since each current value of the HI that is used for predictions from June to the following May is taken from the February-March SLPA. For example, for predictions starting in January, the current HI value can be used until the nearest May; further, according to the suggested model (1), we must use the new HI value, which remains unknown until the coming March. Thus, there is an area in the lead time - target month plane where the forecast using the HI forcing is impossible; this area is masked with a transparent matte overlay in Fig. 3a. An apparent option for optimal forecasting in this area is to use the optimal model without HI forcing (i.e., the AR(2) model with periodic coefficients) in those months where the forcing is unknown during the multimonth iterative predictions.

As observed in Fig. 3a, in general, the prediction skills of the model are improved with the involvement of the forcing. In particular, the model with the seasonal forcing yields lower r.m.s. forecast errors as well as higher correlations between the forecast and reality at lead times up to 6-7 months. The addition of the HI forcing to the seasonally forced model strongly improves the multimonth forecasts with lead times greater than 4 months (where the HI forcing is available) for all target months.

To distinguish the areas where the improvements associated with the HI forcing are significant, we perform an additional statistical test to reject the hypothesis that the prediction skills of the optimal model with the combined seasonal and HI forcing are not better than those of the model with the seasonal forcing alone. Using the AR model with the optimal lag and periodic parameters, we generate 1000 surrogate Niño 3.4 time series representing the ensemble corresponding to the null hypothesis. Then, we learn the optimal model with the combined forcing on each surrogate and calculate the metrics (3). The areas of rejecting the null hypothesis at significance levels of 0.1 and 0.35 are marked by the contours in Fig. 3a for both metrics, e and r. We find that the most significant improvement in the prediction skills lies in the period from August to March for the forecast error e and the entire ENSO cycle from June to May for the correlation r. The lead times of the improved forecasts (1-3 months for the beginning of the cycle and over 12 months for the end of the cycle) can be explained by the intervals between the February-March season used to determine the HI and the target months. This is consistent with the hypothesis that the February-March SLP in the HI region contains useful information about the entire ENSO cycle.

Fig. 3b additionally illustrates the benefits from using the HI in forecasts starting in spring (see also the more detailed Fig. S3 in the SI): while the optimal model with-

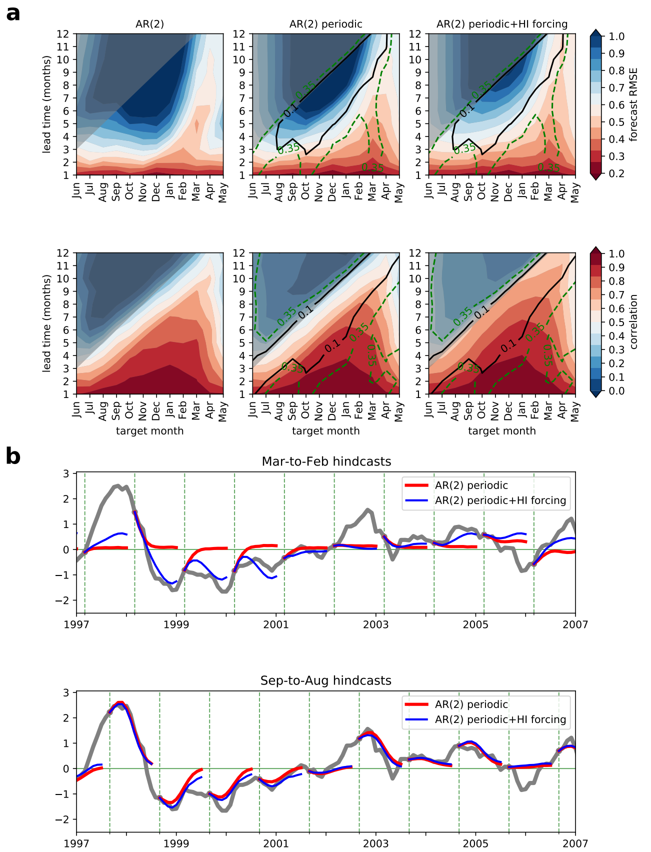

Figure 3. Improving statistical forecasts of the Niño 3.4 index due to the HI forcing. (a) Prediction skills of three statistical models. From left to right: the AR model without forcing with the optimal lag $l = 2$, the AR model with the seasonal forcing with the optimal structural parameters $l = 2$ and $q = 1$, and the optimal AR model ($l = 2$) with the combined seasonal ($q = 1$) and HI forcing. The r.m.s. forecast error (RMSE) e (normalized to the r.m.s. deviation of the detrended Niño 3.4 index, upper panels) and the correlations r (bottom panels) are shown in different target months for lead times from 1 to 12 months. The area where the HI forcing is unavailable is overlain by a transparent matte mask; in the right panels (the HI-forced model), this area is filled using the outputs of the AR(2) model with the seasonal forcing in months with an unknown HI. The contours in the middle and right panels bound the areas of significant improvements of the optimal HI-forced model prediction skills relative to the AR(2) model with the seasonal forcing alone (see the text). The left-tailed test is used for the metric e, and the right-tailed test is used for the metric r. (b) Examples of 12-month hindcasts starting from March (upper panel) and September (bottom panel): the original Niño 3.4 index (gray), outputs of the model with the seasonal forcing only (red) and the model with the combined seasonal and HI forcing (blue).

out the HI forcing tends to predict near zero Niño 3.4 beyond the SPB, the forced model yields much more informative output. In contrast, the forecasts starting long before the SPB (e.g., in autumn) are almost the same for both models.

4 Conclusion

The HI derived from the SLP in February-March is shown to hold important information for the upcoming ENSO cycle lasting from summer to spring of the next year. This information reflects the impacts of the spring patterns of atmospheric circulation anomalies on the summer tropical ocean-atmosphere system due to the SST footprinting mechanism. Thus, the HI can serve as an early predictor for ENSO across the SPB. We demonstrate that the statistical AR model of the Niño 3.4 index taking the HI as a forcing is better in the Bayesian sense and delivers significantly better multimonth predictions. In fact, the HI forcing in the model substantially lowers the SPB and hence increases the predictability of the whole June-May ENSO cycle for forecasts starting in spring. Thus, we can recommend that modelers test the HI as an additional predictor in statistical ENSO models. Further, we will add this forcing into our nonlinear SST-based ENSO model (Gavrilov et al., 2019) included in the IRI/CPC ENSO Predictions Plume (the model is named “IAP-NN” in the plume) and analyze the corresponding gain in its predictive power.

Acknowledgments

NCEP Reanalysis data were provided by the NOAA/OAR/ESRL PSL, Boulder, Colorado, USA, from their website at https://psl.noaa.gov/. The ERSST dataset was downloaded from the NOAA National Centers for Environmental Information (Huang et al., 2017b). This research was supported by the Russian Science Foundation (Contract 19-42-04121) [Constructing the Optimal Niño 3.4 Model with Forcing; Section 3] and the Russian Foundation for Basic Research (grant 19-02-00502) [Finding an Atmospheric ENSO Predictor; Section 2]. The authors thank Professor A. M. Feigin from the Institute of Applied Physics, RAS, for fruitful discussions, as well as an anonymous reviewer, whose suggestions helped to improve the manuscript.

References

Barnston, A. G., Tippett, M. K., L’Heureux, M. L., Li, S., & DeWitt, D. G. (2012, 05). Skill of Real-Time Seasonal ENSO Model Predictions during 200211: Is Our Capability Increasing? *Bulletin of the American Meteorological Society*, *93*(5), 631-651. Retrieved from `https://doi.org/10.1175/BAMS-D-11-00111.1` doi: 10.1175/BAMS-D-11-00111.1

Burgers, G., Jin, F.-F., & van Oldenborgh, G. J. (2005). The simplest enso recharge oscillator. *Geophysical Research Letters*, *32*(13). Retrieved from `https://agupubs.onlinelibrary.wiley.com/doi/abs/10.1029/2005GL022951` doi: 10.1029/2005GL022951

Fang, X. H., & Mu, M. (2018, dec). Both air-sea components are crucial for El Niño forecast from boreal spring. *Scientific Reports*, *8*(1), 1–8. Retrieved from `www.nature.com/scientificreports/` doi: 10.1038/s41598-018-28964-z

Galanti, E., & Tziperman, E. (2000, 09). ENSOs Phase Locking to the Seasonal Cycle in the Fast-SST, Fast-Wave, and Mixed-Mode Regimes. *Journal of the Atmospheric Sciences*, *57*(17), 2936-2950. Retrieved from `https://doi.org/10.1175/1520-0469(2000)057<2936:ESPLTT>2.0.CO;2` doi: 10.1175/1520-0469(2000)057⟨2936:ESPLTT⟩2.0.CO;2

Gavrilov, A., Loskutov, E., & Mukhin, D. (2017). Bayesian optimization of empirical model with state-dependent stochastic forcing. *Chaos, Solitons and Fractals*, *104*, 327–337. Retrieved from `http://www.sciencedirect.com/science/article/pii/S0960077917303648` doi: 10.1016/j.chaos.2017.08.032

Gavrilov, A., Mukhin, D., Loskutov, E., Volodin, E., Feigin, A., & Kurths, J. (2016). Method for reconstructing nonlinear modes with adaptive structure from multidimensional data. *Chaos*, *26*(12). Retrieved from `http://dx.doi.org/10.1063/1.4968852` doi: 10.1063/1.4968852

Gavrilov, A., Seleznev, A., Mukhin, D., Loskutov, E., Feigin, A., & Kurths, J. (2019, feb). Linear dynamical modes as new variables for data-driven ENSO forecast. *Climate Dynamics*, *52*(3-4), 2199–2216. Retrieved from `http://link.springer.com/10.1007/s00382-018-4255-7` doi: 10.1007/s00382-018-4255-7

Hannachi, A., & Iqbal, W. (2019). On the nonlinearity of winter northern hemisphere atmospheric variability. *Journal of the Atmospheric Sciences*, *76*(1), 333-356. Retrieved from `https://doi.org/10.1175/JAS-D-18-0182.1` doi: 10.1175/JAS-D-18-0182.1

Huang, B., Thorne, P. W., Banzon, V. F., Boyer, T., Chepurin, G., Lawrimore, J. H., … Zhang, H.-M. (2017a, 09). Extended Reconstructed Sea Surface Temperature, Version 5 (ERSSTv5): Upgrades, Validations, and Intercomparisons. *Journal of Climate*, *30*(20), 8179-8205. Retrieved from `https://doi.org/10.1175/JCLI-D-16-0836.1` doi: 10.1175/JCLI-D-16-0836.1

Huang, B., Thorne, P. W., Banzon, V. F., Boyer, T., Chepurin, G., Lawrimore, J. H., … Zhang, H.-M. (2017b). *Noaa extended reconstructed sea surface temperature (ersst), version 5.* NOAA National Centers for Environmental Information. doi: 10.7289/V5T72FNM

Jan van Oldenborgh, G., Balmaseda, M. A., Ferranti, L., Stockdale, T. N., & Anderson, D. L. T. (2005, 08). Did the ECMWF Seasonal Forecast Model Outperform Statistical ENSO Forecast Models over the Last 15 Years? *Journal of Climate*, *18*(16), 3240-3249. Retrieved from `https://doi.org/10.1175/JCLI3420.1` doi: 10.1175/JCLI3420.1

Jin, F.-F. (1997, 04). An Equatorial Ocean Recharge Paradigm for ENSO. Part I: Conceptual Model. *Journal of the Atmospheric Sciences*, *54*(7), 811-829. Retrieved from `https://doi.org/10.1175/1520-0469(1997)054<0811:AEORPF>2.0.CO;2` doi: 10.1175/1520-0469(1997)054⟨0811:AEORPF⟩2.0.CO;2

Kalnay, E., Kanamitsu, M., Kistler, R., Collins, W., Deaven, D., Gandin, L., … Joseph, D. (1996, 03). The NCEP/NCAR 40-Year Reanalysis Project. *Bulletin of the American Meteorological Society*, *77*(3), 437-472. Retrieved from `https://doi.org/10.1175/1520-0477(1996)077<0437:TNYRP>2.0.CO;2` doi: 10.1175/1520-0477(1996)077⟨0437:TNYRP⟩2.0.CO;2

Kondrashov, D., Kravtsov, S., Robertson, A. W., & Ghil, M. (2005, 11). A Hierarchy of Data-Based ENSO Models. *Journal of Climate*, *18*(21), 4425-4444. Retrieved from `https://doi.org/10.1175/JCLI3567.1` doi: 10.1175/JCLI3567.1

Kramer, M. A. (1991, feb). Nonlinear principal component analysis using autoassociative neural networks. *AIChE Journal*, *37*(2), 233–243. Retrieved from `http://doi.wiley.com/10.1002/aic.690370209` doi: 10.1002/aic.690370209

Liu, Z., Jin, Y., & Rong, X. (2018, 12). A Theory for the Seasonal Predictability Barrier: Threshold, Timing, and Intensity. *Journal of Climate*, *32*(2), 423-443.

Retrieved from https://doi.org/10.1175/JCLI-D-18-0383.1 doi: 10.1175/JCLI-D-18-0383.1

McPhaden, M. J. (2003). Tropical pacific ocean heat content variations and enso persistence barriers. *Geophysical Research Letters*, *30*(9). Retrieved from https://agupubs.onlinelibrary.wiley.com/doi/abs/10.1029/2003GL016872 doi: 10.1029/2003GL016872

Mukhin, D., Gavrilov, A., Feigin, A., Loskutov, E., & Kurths, J. (2015). Principal nonlinear dynamical modes of climate variability. *Scientific Reports*, *5*, 15510. Retrieved from http://www.nature.com/articles/srep15510 doi: 10.1038/srep15510

Mukhin, D., Gavrilov, A., Loskutov, E., Feigin, A., & Kurths, J. (2018, sep). Nonlinear reconstruction of global climate leading modes on decadal scales. *Climate Dynamics*, *51*(5-6), 2301–2310. Retrieved from http://link.springer.com/10.1007/s00382-017-4013-2 doi: 10.1007/s00382-017-4013-2

Newman, M., & Sardeshmukh, P. D. (2017). Are we near the predictability limit of tropical indo-pacific sea surface temperatures? *Geophysical Research Letters*, *44*(16), 8520-8529. Retrieved from https://agupubs.onlinelibrary.wiley.com/doi/abs/10.1002/2017GL074088 doi: 10.1002/2017GL074088

Schwarz, G. (1978, 03). Estimating the dimension of a model. *Ann. Statist.*, *6*(2), 461–464. Retrieved from https://doi.org/10.1214/aos/1176344136 doi: 10.1214/aos/1176344136

Suarez, M. J., & Schopf, P. S. (1988, 11). A Delayed Action Oscillator for ENSO. *Journal of the Atmospheric Sciences*, *45*(21), 3283-3287. Retrieved from https://doi.org/10.1175/1520-0469(1988)045<3283:ADAOFE>2.0.CO;2 doi: 10.1175/1520-0469(1988)045⟨3283:ADAOFE⟩2.0.CO;2

Timmermann, A., An, S. I., Kug, J. S., Jin, F. F., Cai, W., Capotondi, A., … Zhang, X. (2018, jul). *El NiñoSouthern Oscillation complexity* (Vol. 559) (No. 7715). Nature Publishing Group. Retrieved from https://www.nature.com/articles/s41586-018-0252-6 doi: 10.1038/s41586-018-0252-6

Tippett, M. K., & L'Heureux, M. L. (2020, dec). Low-dimensional representations of Niño 3.4 evolution and the spring persistence barrier. *npj Climate and Atmospheric Science*, *3*(1), 1–11. Retrieved from https://doi.org/10.1038/s41612-020-0128-y doi: 10.1038/s41612-020-0128-y

Torrence, C., & Webster, P. J. (1998). The annual cycle of persistence in the el no/southern oscillation. *Quarterly Journal of the Royal Meteorological Society*, *124*(550), 1985-2004. Retrieved from https://rmets.onlinelibrary.wiley.com/doi/abs/10.1002/qj.49712455010 doi: 10.1002/qj.49712455010

Vimont, D. J., Alexander, M., & Fontaine, A. (2009, 02). Midlatitude Excitation of Tropical Variability in the Pacific: The Role of Thermodynamic Coupling and Seasonality*. *Journal of Climate*, *22*(3), 518-534. Retrieved from https://doi.org/10.1175/2008JCLI2220.1 doi: 10.1175/2008JCLI2220.1

Vimont, D. J., Wallace, J. M., & Battisti, D. S. (2003, 08). The Seasonal Footprinting Mechanism in the Pacific: Implications for ENSO*. *Journal of Climate*, *16*(16), 2668-2675. Retrieved from https://doi.org/10.1175/1520-0442(2003)016<2668:TSFMIT>2.0.CO;2 doi: 10.1175/1520-0442(2003)016⟨2668:TSFMIT⟩2.0.CO;2

Yu, J.-Y., & Fang, S.-W. (2018). The distinct contributions of the seasonal footprinting and charged-discharged mechanisms to enso complexity. *Geophysical Research Letters*, *45*(13), 6611-6618. Retrieved from https://agupubs.onlinelibrary.wiley.com/doi/abs/10.1029/2018GL077664 doi: 10.1029/2018GL077664